Journal of Physics D: Applied Physics

PAPER • **OPEN ACCESS**

Synergy of experiment and model for reactive HiPIMS: effect of discharge parameters on WO_x composition and deposition rate

To cite this article: J Rezek *et al* 2021 *J. Phys. D: Appl. Phys.* **54** 125202

OPEN ACCESS
IOP Publishing
Journal of Physics D: Applied Physics
J. Phys. D: Appl. Phys. **54** (2021) 125202 (11pp)
https://doi.org/10.1088/1361-6463/abd1a3

Synergy of experiment and model for reactive HiPIMS: effect of discharge parameters on WO_x composition and deposition rate

J Rezek, T Kozák, N Kumar and S Haviar

Department of Physics and NTIS, European Centre of Excellence, University of West Bohemia, Univerzitní 8, 306 14, Plzeň, Czech Republic

E-mail: jrezek@ntis.zcu.cz

Received 1 October 2020, revised 19 November 2020
Accepted for publication 8 December 2020
Published 19 January 2021

Abstract

Reactive high-power impulse magnetron sputtering of tungsten oxide films using metallic tungsten target (72 mm in diameter) in argon-oxygen atmosphere (total pressure of 0.75 Pa) was carried out. The effect of various discharge parameters on the deposition rate and film oxygen concentration was investigated. Moreover, a model combining a reactive high-power impulse magnetron sputtering model and a discharge plasma model for the ionization region was successfully used for deeper insight into the effect of particular discharge parameters such as voltage pulse length (from 100 –800 μs), oxygen partial pressure (from 0.25–0.50 Pa) or the value of pulse-averaged target power density (from 2.5–500 W cm^{-2}). The results of the presented model, most notably trends in the target- and substrate oxide fraction, composition of particle fluxes onto the substrate, degree of W atom ionization or degree of O_2 molecule dissociation are discussed and put into context with experimentally measured quantities.

Keywords: reactive HiPIMS model, deposition rate, tungsten oxide

(Some figures may appear in colour only in the online journal)

1. Introduction

In the field of thin-film research and development, reactive high-power impulse magnetron sputtering (r-HiPIMS) has become the centre of attention in recent years. This is thanks to the ability of this technique to produce densified, high-quality defect-free oxide, nitride and oxynitride coatings [1–6]. The maximization of the deposition rate during r-HiPIMS has also been studied intensively and many approaches allow one to produce thin films at high deposition rates without sacrificing film quality [7, 8]. Much attention is also devoted to the investigation of processes connected with the presence of reactive gas (RG, typically oxygen and/or nitrogen) in the gas mixture and its interaction with the target and substrate surface. There are a few theoretical models describing the complex behaviour of r-HiPIMS plasma discharge that have been developed. In order to be applicable to high-power impulse magnetron sputtering (HiPIMS) discharge conditions, the models of conventional reactive sputtering (e.g. [9–14]) were extended to account (especially) for the ionization and return of sputtered metal atoms onto the target [15–19] and the dissociation of RG in the discharge plasma [15, 16, 19]. Some of those models simulated mainly the composition of the reactive surfaces and the balance of RG in the discharge chamber and the hysteresis effect [17, 20], while another focused on the simulation of the

discharge plasma during the pulse for a fixed composition of the reactive surfaces [19].

However, there are a lack of publications focused on the deeper understanding of the effects responsible for different film stoichiometry under different discharge conditions (namely voltage pulse length, pulse-averaged target power density, RG partial pressure,etc). In this publication, we clarify the relation between the abovementioned discharge parameters and WO_x properties, namely the deposition rate and oxygen content in the film. We have chosen the W-O system since WO_3 is a material that is in demand due to its many potential applications such as the active layer of hydrogen gas sensors [21, 22] and as part of electrochromic [23, 24] or gasochromic [25] devices. Moreover, tungsten oxide is a convenient choice thanks to its relatively high electrical conductivity that provides fair discharge stability. A new model of the reactive sputtering process was used to calculate the oxide coverage of the target and substrate, the deposition rate of films and other discharge parameters based on the experimental current–voltage waveforms. For the first time, this model combines an r-HiPIMS model [15] and a discharge plasma model for the ionization region (IR) in front of the sputtered target [26]. By comparing the simulated and experimental results and by evaluating the discharge parameters that cannot be easily measured, we explain the observed experimental trends.

2. Methodology

2.1. Film preparation

The tungsten oxide films were deposited using HiPIMS sputtering from a tungsten target with a diameter of 72 mm in a stainless-steel vacuum chamber (Leybold-Heraeus LH Z400) pumped by a turbomolecular pump (backed with a scroll pump) and a cold trap (cooled by liquid nitrogen). The magnetron was powered by a unipolar HiPIMS power supply (SIPP2000_USB, Melec GmbH). The base pressure before each deposition was below 1 mPa. The substrate-to-target distance was 70 mm. The depositions were carried out in a mixture of argon and oxygen. The working pressure was set to a constant value of 0.75 Pa. The average target power density was kept constant for all experiments (2.35 W cm^{-2}). During the experiments, the values of the oxygen partial pressure, p_{ox}, voltage pulse length, t_{on}, and/or pulse-averaged target power density, S_{da}, were varied.

All specimens were prepared on $10 \times 10\,mm^2$ Si (100) substrates (625 μm thick). Before the deposition, the substrates were cleaned by sonication for 5 min in demineralized water and then isopropyl alcohol. The thickness of the films was within the range of 800–1000 nm.

2.2. Film characterization

The elemental composition of WO_x films was measured by wavelength-dispersive spectroscopy (WDS, Magnaray ThermoScientific) conducted in the chamber of a scanning electron microscope (SEM, Horiba, SU-70). The used primary electron energy was 10 keV, the standards of pure tungsten metal (99.95% purity) and hematite (Fe_2O_3, 99.97 purity) (Astimex Standards) were used for the quantification of W and O, respectively. For comparison with the model, it is important that the precision of the WDS method can be considered below 1 at.% for both W and O content. The trueness of our measurement, though, can be accurately estimated to be about 3 at.%, but this does not affect the observed trends. The deposition rate was calculated as the film thickness to deposition time ratio. The thickness was evaluated from SEM cross-sectional images.

2.3. The r-HiPIMS model

An r-HiPIMS model was used to simulate the HiPIMS deposition processes to gain more insight into the process parameters that are difficult to measure experimentally and to explain the measured dependencies. The model has two parts: (a) a model describing the time evolution of RG partial pressure and the composition of relevant surfaces (target, substrate and chamber walls), and (b) an IR model describing the time evolution of relevant plasma species densities in the region in front of the magnetron (IR) where the electrons are trapped by the magnetic field of the magnetron. Thus, this region is most relevant for capturing the ionization and RG dissociation processes in the discharge plasma. A schematic representation of the model is shown in figure 1.

The composition of the target, substrate and chamber walls is described using compound fraction Θ, which is the fraction of surface covered by stoichiometric compound ($\Theta = 0$ for pure metal while $\Theta = 1$ for stoichiometric compound) as in the well-known Berg model [9]. The compound fraction is calculated from balance equations of the form:

$$n_0 h x_c \frac{d\Theta}{dt} = \sum_j \Gamma_j, \qquad (1)$$

where n_0 is the atomic density of the target material (pure metal), h is the layer thickness for which its composition is simulated (~one monolayer), x_c is the stoichiometry of the compound, i.e. the number of oxygen atoms for each metal atom in the compound, Θ is the compound fraction in the layer and Γ_j is the flux of oxygen atoms to or from the layer. The right-hand side accounts for all the processes changing the compound fraction, such as sputtering, chemisorption and ion implantation for the target, and deposition of sputtered atoms and chemisorption on the substrate and chamber walls. The ionization of the sputtered atoms and subsequent return and implantation into the target is also included. This was confirmed to be critical in r-HiPIMS where the probability of ionization of sputtered atoms is high [27]. This part of the model is based on our previous work [15, 16] where you can find more details about the model description of the balance equations. In this work, the model was extended by (a) adding the balance equation for the RG partial pressure in the vacuum chamber and (b) including several equidistant target layers allowing us to improve the accuracy of modelling the ion implantation. The former accounts for all gains and losses of RG molecules

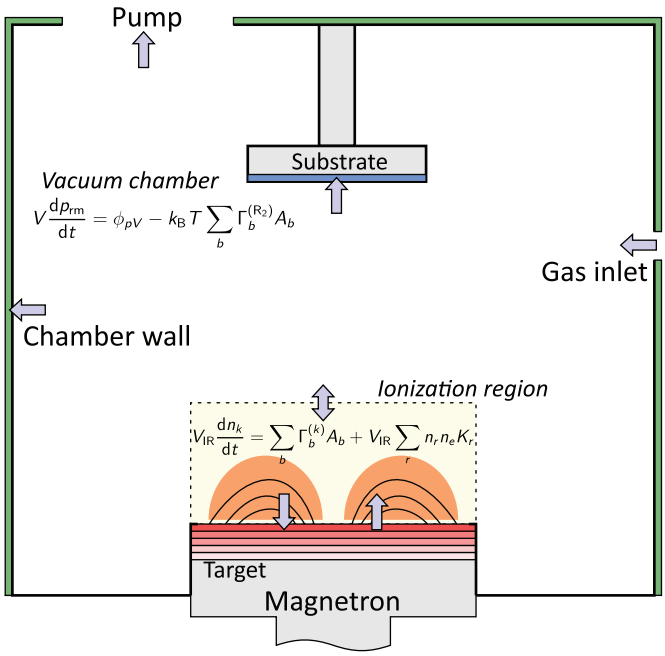

Figure 1. Scheme of the r-HiPIMS model. The model calculates (a) the fraction of reactive compound in several target layers (shown in red) and on the surface of the substrate (blue) and the chamber walls (green), (b) densities of plasma species (neutrals and ions) in the IR and (c) the partial pressure of RG in the vacuum chamber. The model also evaluates the fluxes of plasma species to and from the target and onto the substrate (indicated by arrows). Symbols are defined in the text.

in the vacuum chamber and allows us to calculate the RG partial pressure for a varying RG flow rate. The latter allows us to calculate a depth-resolved composition of the target. Strict mass conservation is enforced for the target layers that are coupled by the transport of material between them. As the target material is sputtered away from the target surface, the oxygen in the target is moved across the layers towards the target surface. On the other hand, when target material ions are implanted into the target, the oxygen in the target layers below the depth of implantation is moved deeper into the target.

The IR model calculates the plasma species densities in the IR during a period of the HiPIMS pulse. This is a volume-averaged model assuming constant densities in the IR, similar to our previous work [26]. The species include Ar, M, R_2, R, R_s, Ar^+, M^+, $R_2{}^+$ and R^+, where M stands for the sputtered metal atom, R_2 for the RG molecule, R for the RG atom and R_s for the (fast) RG atom sputtered from the target. The IR model equations have the form:

$$V_{\mathrm{IR}} \frac{\mathrm{d}n_k}{\mathrm{d}t} = \sum_b \Gamma_b^{(k)} A_b + V_{\mathrm{IR}} \sum_r n_r n_e K_r (T_e), \qquad (2)$$

where the left-hand side is the number change of species k in the IR, the first term on the right-hand side accounts for changes due to the transport of particles from the IR and the second term accounts for the change of particle density due to reactions (mainly, but not exclusively, those involving electrons). A necessary parameter of the IR model is the fraction of ions created in the IR that return onto the target. This return probability, β, is assumed to be constant and equal for all species. As the rate of ionization of neutral species depends on the electron temperature, T_e, and the ion density determines the ion current onto the target, the model uses a known (user input) target current waveform to calculate $T_e(t)$ assuming a known (constant) secondary electron emission yield. This $T_e(t)$ then determines all the electron reaction constants in the particle balance equations. The two parts of the simulation are coupled together as follows. The RG partial pressure and the compound fractions on the target, substrate and chamber walls calculated for a given time by the reacting surface model enter the IR model. They are assumed to be constant during a single HiPIMS pulse period, see [15, 28]. The IR model then provides the densities of species in the IR and the corresponding total fluxes of species onto the target, substrate and chamber walls, which are used in the model for the reactive surfaces. Thus, the two parts of the model are solved repeatedly with mutual exchange of data to integrate in time. It should be noted that due to the significantly different characteristic time scales of the two models (typically μs for the IR model compared to ms or longer for the reactive surface model), it is not reasonable to solve the coupled equations of both models simultaneously.

In the present paper, the model is used to simulate depositions of WO_3. The geometrical parameters of the model, such as the chamber volume, target diameter and target–substrate distance were set according to the experiments. The oxygen partial pressure is set constant as in the experiments, with the total pressure always 0.75 Pa. The necessary material parameters of the model were set according to table 1. The sputtering yield of W from a W target, Y_{mm}, and the implantation depth profiles for W and O atoms into a W target (not included in the table) were calculated by SDTrimSP [29] as a function of ion energy. Due to the lack of reliable data for sputtering yields from the compound targets, we assumed that the sputtering

Table 1. Parameters related to the target material (W) used by the reactive model. E is the energy of ions incident on the target, Θ_t is target oxide fraction.

Parameter	Value	Unit
W density	19.24	g cm^{-3}
WO_3 density	7.16	g cm^{-3}
O_2 sticking coefficient on W	0.03	
O sticking coefficient on W	1.0	
W sputtering yield from W, Y_{mm}, by Ar^+	$\frac{3.72\left(\frac{E}{71}-1\right)^{1.01}}{22.3+\left(\frac{E}{71}-1\right)^{1.01}}$	
W sputtering yield from W, Y_{mm}, by W^+	$\frac{4.12\left(\frac{E}{100}-1\right)^{1.3}}{27.0+\left(\frac{E}{100}-1\right)^{1.3}}$	
W sputtering yield from W, Y_{mm}, by O^+	$\frac{1.23\left(\frac{E}{78}-1\right)^{1.05}}{13.9+\left(\frac{E}{78}-1\right)^{1.05}}$	
W sputtering yield as function of Θ_t	$Y_{\mathrm{mm}}\left(1-\Theta_t+\frac{\Theta_t}{7}\right)$	
O sputtering yield as function of Θ_t	$Y_{\mathrm{mm}}\Theta_t$	
Ion return probability	0.6	
Gas temperature	300	K

Table 2. Summary of reactions implemented in the discharge plasma model for the IR.

Reaction	Rate constant ($m^{-3}s^{-1}$)	Reference
$e + Ar \rightarrow 2e + Ar^+$	$2.34 \times 10^{-14} T_e^{0.59} e^{-\frac{17.4}{T_e}}$	[34]
$e + W \rightarrow 2e + W^+$	$5.61 \times 10^{-14} T_e^{0.58} e^{-\frac{9.82}{T_e}}$	Calculated from the cross-section from [35]
$e + O_2 \rightarrow 2e + O_2^+$	$2.34 \times 10^{-15} T_e^{1.03} e^{-\frac{12.3}{T_e}}$	[36]
$e + O_2 \rightarrow e + 2O$	$6.86 \times 10^{-15} e^{-\frac{6.29}{T_e}}$	[34]
$e + O_2^+ \rightarrow 2O$	$2.2 \times 10^{-14} T_e^{-0.5}$	[37]
$e + O_2 \rightarrow 2e + O + O^+$	$1.88 \times 10^{-16} T_e^{1.70} e^{-\frac{16.8}{T_e}}$	[36]
$e + O \rightarrow 2e + O^+$	$9.0 \times 10^{-15} T_e^{0.7} e^{-\frac{13.6}{T_e}}$	[38]

yield of W from WO_3, $Y_{mc} = Y_{mm}/7$, and the sputtering yield of O from WO_3, $Y_{rc} = 7\ Y_{mc}$, to take into account preferential sputtering of O from WO_3 [30]. These fixed values were estimated based on a comparison of experimental and simulated deposition rates of WO_3 and W. The sputtering yield at arbitrary compound fraction Θ_t, is calculated by linear interpolation between the sputtering yields from W and WO_3. The ion return probability is an unknown parameter for the simulated discharge setup. We tested a broad range of values from 0.3–0.9 based on the paper [31] where possible values of the ion return probability span this range depending on the target voltage. The value of 0.6 was used for the final series of calculations in the hope that this is a reasonable mean value suitable for all analyzed regimes, although [32, 33] suggest values closer to our upper limit of 0.9. As will be shown in the results, the particular value of the ion return probability has a weak effect on the modelling results.

The reactions in the discharge plasma and the corresponding reaction rate constants are summarized in table 2. The model is calculated from initial conditions until a steady state is reached that corresponds to the deposition-averaged conditions obtained in the experiments.

To summarize, the model uses experimental geometry, current and voltage waveforms, Ar and oxygen flow rate or partial pressure, ion return probability and other material parameters (densities, sticking coefficients, sputtering yields, implantation profiles) as input. It solves balance equations for several plasma species in the IR of the discharge plasma and balance equations for oxygen in the target, substrate, chamber walls and chamber volume. Most notably, the model takes into account (a) the ionization of sputtered atoms and the dissociation of oxygen in the discharge plasma and calculates those based on the electron density and temperature, (b) the dissociation of oxygen in the discharge and different sticking coefficients for oxygen atoms and molecules, (c) chemisorption as well as implantation of oxygen into the target and (d) the return of ionized sputtered atoms onto the target and their implantation into subsurface layers of the target. The model is used to calculate the composition of the target and substrate, deposition rate of films and densities of species in the discharge plasma.

Finally, we mention the limitations of the current model. The model is based on the volume-averaged approach (assumes homogeneous density in the IR and homogeneous oxide fraction in the studied surfaces). Thus, it does not resolve spatial inhomogeneities of the calculated quantities and is inherently less accurate than any spatially resolved simulation. Therefore, negative ions are not included now, although their role in r-HiPIMS has been studied [39]. Some of the material parameters such as sputtering yields and sticking coefficients are not well known and can vary significantly based on fine details of the experimental system. Therefore, the absolute values of the calculated quantities should be taken with a pinch of salt. Instead, we focus on observing the trends and make conclusions based on the comparison of model results among different regimes. The oxide fraction Θ is inherently limited to values $\Theta < 1$, and for oxygen-rich conditions, Θ slowly approaches unity. Therefore, in contrast to reality, the model cannot give over-stoichiometric composition of a surface, and, for compositions close to the stoichiometric oxide, the corresponding Θ is likely to be underestimated. The deposition rate of films was calculated from the flux of W atoms onto the substrate assuming a fixed density of the film equal to the density of the stoichiometric oxide, while in reality the density of films is expected to vary with the exact film composition. These limitations of the model will be considered in the ongoing discussion.

3. Results and discussion

In the following, we present the experimentally measured and calculated deposition rate and oxygen content in the film obtained under different deposition conditions. Phenomena determining the observed trends are explained using different model output quantities, such as target- and substrate oxide fraction, degree of O_2 dissociation, degree of W atom ionization, composition of particle flux onto the substrate or time evolution of particle densities in front of the target. First, we discuss the different behaviour of the reactive DC and HiPIMS processes. Next, we report on the effect of pulse-averaged target power density on the abovementioned quantities. In the last section, we discuss the effect of the voltage pulse length at a constant pulse-averaged target power density.

3.1. Comparison of DC and HiPIMS discharge regimes

In figure 2, a comparison of the deposition rate (a) and oxygen content in the film (b) as a function of p_{ox} is shown. In the case of DC, the deposition rate decreases with increasing p_{ox}, which is the expected behaviour observed for many target materials. This is explained by the fact that the oxide coverage of the target surface increases with the increasing oxygen partial pressure and, consequently, the sputtering rate of the metal atoms decreases [30, 40]. This is confirmed by the model (not shown), which implements a pre-set dependence of the sputtering yield on the target oxide coverage, Θ_t. This

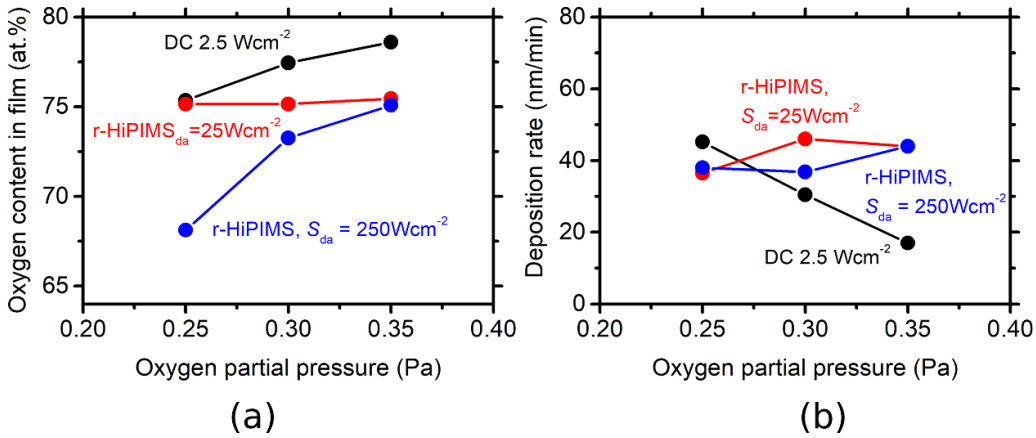

Figure 2. Deposition rate (a), and oxygen content in the film (b) as a function of oxygen partial pressure for three different discharge regimes ($t_{on} = 800$ μs in the case of r-HiPIMS deposition).

is also qualitatively in agreement with the increasing oxygen content in the film, C_{ox}, 75.4 at.% at $p_{ox} = 0.25$ Pa to 78.6 at.% at $p_{ox} = 0.35$ Pa, which is correlated with Θ_s calculated by the model.

In the case of r-HiPIMS, the situation is more complicated. Higher $S_{da} = 250$ W cm^{-2} ('high-power regime') leads to a gradual increase of C_{ox} from 68.1 at.% to 75.1 at.% with increasing p_{ox} (similar to the DC regime), whereas, C_{ox} is almost constant (~75.2 at.%) for the low value of $S_{da} = 25$ W cm^{-2} ('low-power regime'). This is not observed in the model results where Θ_s monotonously increases with the oxygen partial pressure for both $S_{da} = 25$ W cm^{-2} and 250 W cm^{-2}. In contrast to the DC case, there is no decrease in deposition rate for both the low- and high-power regime. Moreover, for p_{ox} of 0.30 and 0.35 Pa, the deposition rate in the HiPIMS case is higher than in the DC case. This potentially surprising result is not entirely unusual. It was also reported by Hemberg *et al* for tungsten oxide [41] and Hála *et al* for niobium oxide [42]. This is primarily caused by a lower oxide fraction on the target (see figure 3). The model results indicate that the oxide coverage of the target decreases with increasing target power density (in a pulse in the case of HiPIMS). Moreover, in figure 3, one of the r-HiPIMS benefits is clearly seen; the Θ_s/Θ_t ratio (at given p_{ox}) increases with increasing S_{da}. This means for higher S_{da} the discharge is close to the desired regime; production of stoichiometric films, while the target is as metallic as possible.

There are several processes that affect Θ_t and they all change simultaneously when the pulse-averaged target power density in a pulse is changed. Figure 4 shows the effect of the ion return probability on the oxide coverage for the DC and high-power regime. It should be noted that realistic values of the ion return probability probably lie in the range of 0.5–0.9 [31, 32]. Overall, for the given conditions, the effect of pre-selected ion return probability is weak and does not change the trends observed, especially the fundamental difference between the DC and HiPIMS case. More specifically, the calculated oxide fraction changes by a few percentage points and the calculated deposition rate (not shown) decreases by 5% in the DC case and 15% for the HiPIMS high-power case

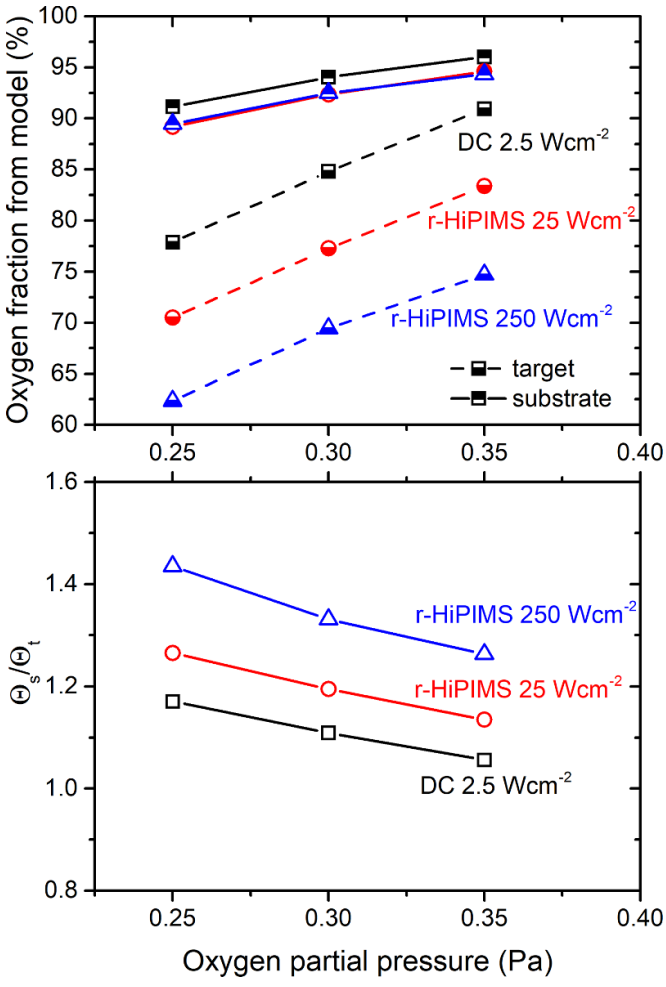

Figure 3. Top panel: calculated oxide fraction on the substrate (half-up symbols) and the target (half-down symbols) as a function of oxygen partial pressure for three different discharge regimes. Bottom panel: calculated ratio of the substrate and target oxide fraction as a function of oxygen partial pressure for three different discharge regimes ($t_{on} = 800$ μs in the case of r-HiPIMS).

when the ion return probability increases from 0.6 to 0.9. In the DC case, Θ_t slightly increases and Θ_s slightly decreases

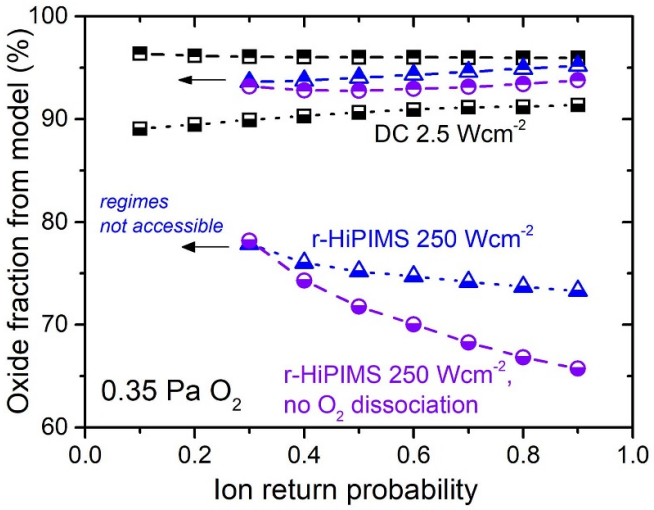

Figure 4. Calculated oxide fraction on the substrate (half-up symbols) and the target (half-down symbols) as a function of the ion return probability calculated for the DC regime (2.5 W cm^{-2}, black symbols) and the high-power regime (S_{da} = 250 W cm^{-2}, t_{on} = 800 μs, blue symbols) and the O_2 partial pressure of 0.35 Pa. In addition, simulation results for the high-power regime with no O_2 dissociation are shown by purple symbols.

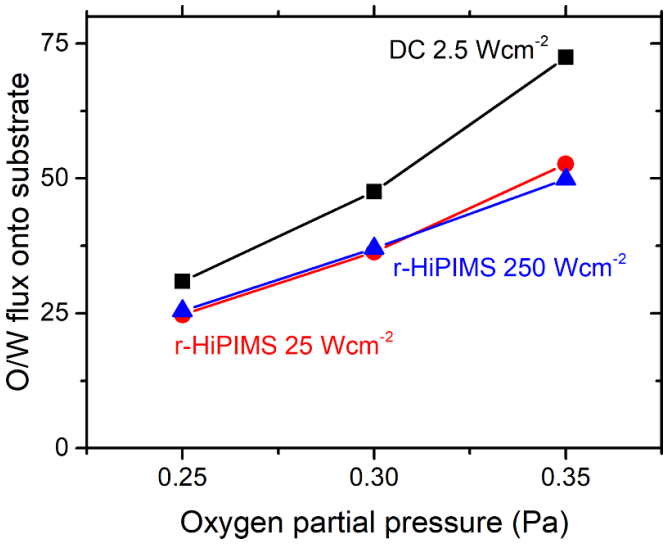

Figure 5. Calculated ratio of oxygen and tungsten particle fluxes (atoms and ions) onto the substrate as a function of oxygen partial pressure for three different discharge regimes (t_{on} = 800 μs in the case of r-HiPIMS deposition).

with an increasing ion return probability. As the sputtering rate of W and its ionization are low in this case, this trend can be explained by the increased attraction of O_2^+ ions and their implantation into the target. On the other hand, in the HiPIMS case, Θ_t decreases and Θ_s increases with the increasing ion return probability, see the blue curves. In this case, the degree of ionization of W in the discharge is high (~70% for S_{da} = 250 W cm^{-2} resulted from the model, not shown) and W^+ ions reimplanted into the target effectively decrease the oxide coverage of the target.

If oxygen dissociation was neglected (see the violet curve), the decrease of Θ_t would be even more pronounced. However, O_2 dissociation increases the reactivity of O atoms generated in the high-density plasma during the pulse and, thus, increases Θ_t and partly compensates the effect of target metallization by W^+ ion implantation (see again the blue curve, which includes both W^+ implantation and O_2 dissociation). Overall, the return of W ions onto the target is a significant factor causing the decrease in Θ_t in r-HiPIMS discharges in agreement with recent studies [27].

As mentioned, a fraction of the sputtered metal atoms returns onto the target as ions. However, there is considerable increased flux left on the substrate, which is not complemented by a sufficiently high flux of O atoms. This leads to a slightly lower Θ_s when compared to the DC case. Figure 5 shows that the ratio of O/W fluxes onto the substrate decreases when the discharge regime is changed from DC to HiPIMS. Here, the difference between the low- and high-power regime is negligible.

As can be observed in figure 6, the current waveform for the high-power regime has a typical shape indicating gas rarefaction [43, 44] in front of the target. Note that this effect is difficult to calculate accurately with a volume-averaged model of the discharge plasma [45] and it cannot be adequately implemented in the present model. In the case of reactive sputtering, not only argon but also RG (oxygen in our case) particles (molecules, atoms and ions) are pushed away from the volume between the target and the substrate and, thus, a lower amount of oxygen particles reacts with the arriving W species on the substrate surface. Therefore, it is suggested that gas rarefaction in r-HiPIMS (especially in the high-power regime) also contributes to the lower oxygen concentration in the films, which is in agreement with the measured film elemental composition, see figure 2(b).

3.2. *Pulse-averaged target power density effect*

In this section, the effects of pulse-averaged target power density (ranged from 100–500 W cm^{-2} at constant t_{on} = 100 μs) on oxygen content in the film and deposition rate will be discussed. Depositions and model calculations were carried out under two different oxygen partial pressures: 0.25 Pa ('low-oxygen regime') and 0.50 Pa ('high-oxygen regime').

Experimentally determined oxygen content in the film, C_{ox}, and model calculations for oxide fraction formed on the substrate and target surface are presented in figure 7. As can be expected, C_{ox} is significantly higher for the high-oxygen regime compared to the low-oxygen regime. With increasing S_{da}, C_{ox} slightly decreases for both low- and high-oxygen regimes, i.e. the film becomes more metallic. In accordance with that, the target surface is also more metallic with increasing S_{da}, as confirmed by the calculated oxide fraction on the target surface (Θ_t), see top panel of figure 7. As expected, the calculated Θ_t is also systematically higher for the high-oxygen regime. On the other hand, the trend for C_{ox} is not fully confirmed by the model; Θ_s is practically constant for the high-oxygen regime, but it slightly increases for the low-oxygen regime. This indicates that the model overestimates

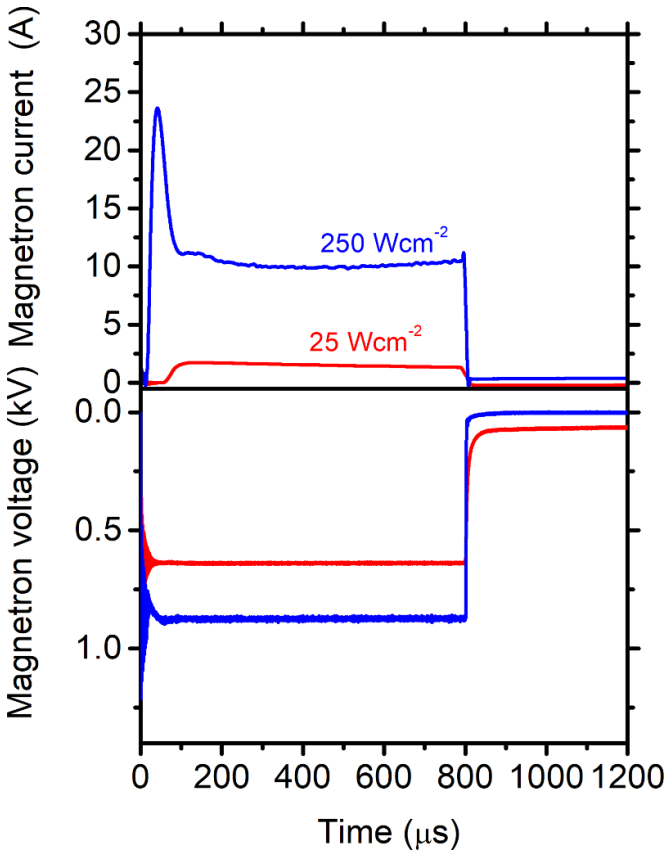

Figure 6. Magnetron current and voltage waveforms for low- and high-power regimes at constant $p_{ox} = 0.35$ Pa.

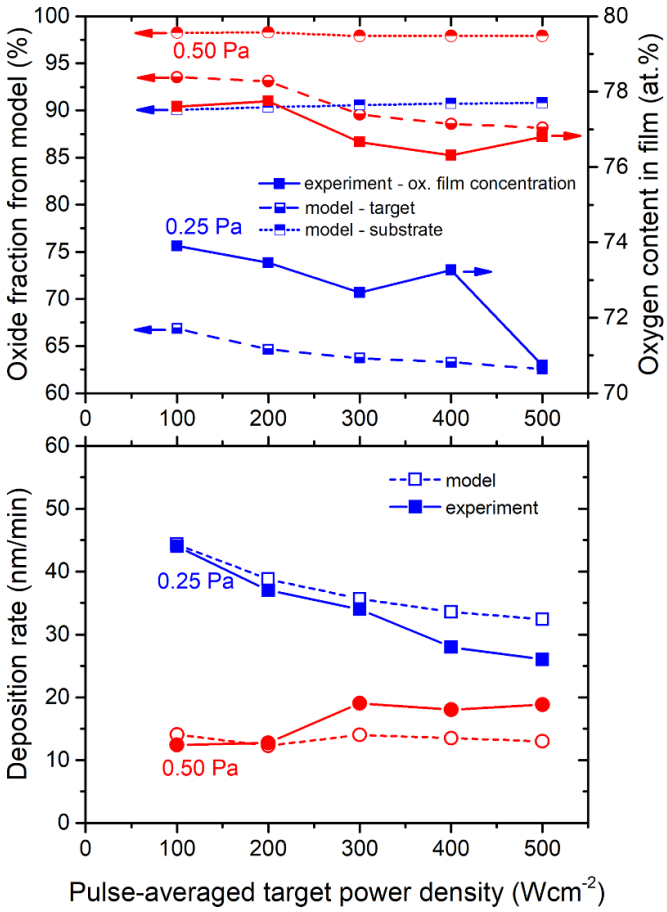

Figure 7. Top panel: calculated oxide fraction (dashed lines) on the substrate (half-up symbols) and the target (half-down symbols) and experimentally measured oxygen content in the film (solid lines) as a function of S_{da} for two values of p_{ox} (0.25 and 0.50 Pa). Bottom panel: calculated (dashed lines) and experimentally measured (solid lines) deposition rate as a function of S_{da} for two values of p_{ox} (0.25 and 0.50 Pa).

the flux of oxygen with respect to the flux of W particles towards the substrate. The bottom panel in figure 7 depicts trends in deposition rate and also shows qualitative compliance between experimentally measured and calculated deposition rates. For the low-oxygen regime, the deposition rate decreases with increasing S_{da}, which is mainly caused by increased ion return onto the target, while the sputtering rate of metals from the target is constant (indicated by the model results, not shown). For the high-oxygen regime, the experimental deposition rate slightly increases with increasing S_{da}, while the calculated deposition rate remains practically constant. This can be explained by the decrease in Θ_t, see figure 7 (top panel), which results in a slight increase in the sputtering rate of metals from the target. At the same time, the change in ion return flux is less pronounced in the presented range of S_{da} values (indicated by the model results, not shown). Figure 8 shows the calculated flux of W and O particles (atoms and ions) onto the substrate. For the high-oxygen regime, the flux of O decreases with increasing S_{da}, while the flux of W remains practically constant. Thus, the O/W flux ratio decreases and, therefore, Θ_s decreases with increasing S_{da}. On the other hand, for the low-oxygen regime, both O and W fluxes decrease and the O/W flux ratio slightly increases leading to the observed increase in Θ_s.

Figure 9 shows the degree of O_2 dissociation and W ionization in front of the target as calculated by the IR model. As expected, we observe an increase in both quantities as S_{da} increases. It is interesting to note that for the high-oxygen regime, the W ionization degree between 200–500 W cm^{-2} does not increase as fast as for the low-oxygen regime. It could be explained by the fact that for the high-oxygen regime, the high fraction of O_2 in the discharge is dissociated ($E_{diss} = 5.15$ eV) and/or ionized, which consumes part of the energy delivered during the pulse, which cannot be used for W ionization ($E_{iz} = 7.86$ eV). Thus, the lower amount of W atoms in the high-oxygen regime (because fewer W atoms are sputtered from the target, see higher Θ_t in figure 7) and the not so high ionization of W leads to lower losses of sputtered W by the ion return effect, resulting in the non-decreasing dependence of the flux of W onto the substrate on S_{da} (figure 8).

The experimentally measured deposition rate decreases from 44 to 26 nm min^{-1}, while it slightly increases from 12 to 19 nm min^{-1} with increasing S_{da} for the low- and high-oxygen regime, respectively. These trends are in very good agreement with the model calculations. The decrease in deposition rate for the low-oxygen regime is well known in non-reactive HiPIMS [46]. Here, it can be mainly attributed to the return of ionized metal atoms onto the target as the degree of ionization

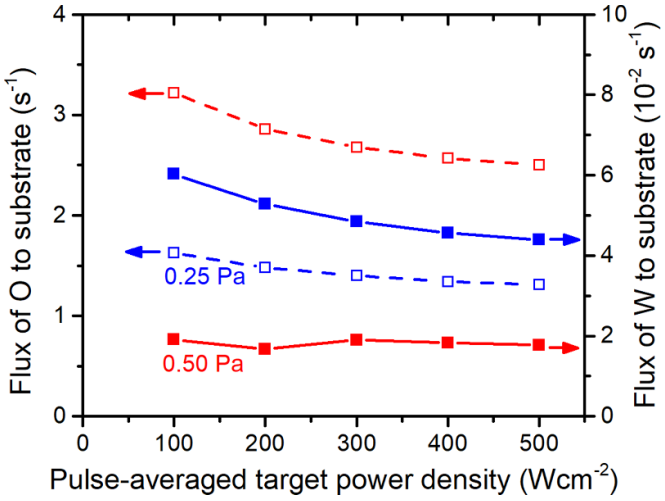

Figure 8. Calculated fluxes of O (dashed lines, empty symbols) and W (solid lines, full symbols) particles (atoms and ions) onto the substrate as a function of the pulse-averaged target power density for the O_2 partial pressure of 0.25 Pa (blue) and 0.50 Pa (red).

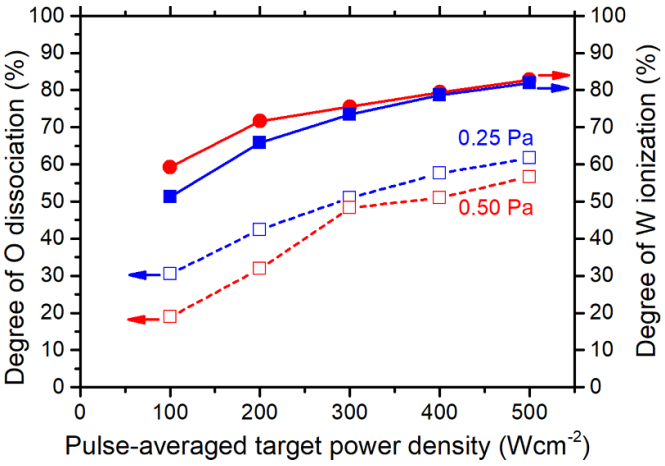

Figure 9. Calculated degree of oxygen molecule dissociation (dashed lines) and tungsten atom ionization (solid lines) as a function of S_{da} for two values of p_{ox} (0.25 and 0.50 Pa).

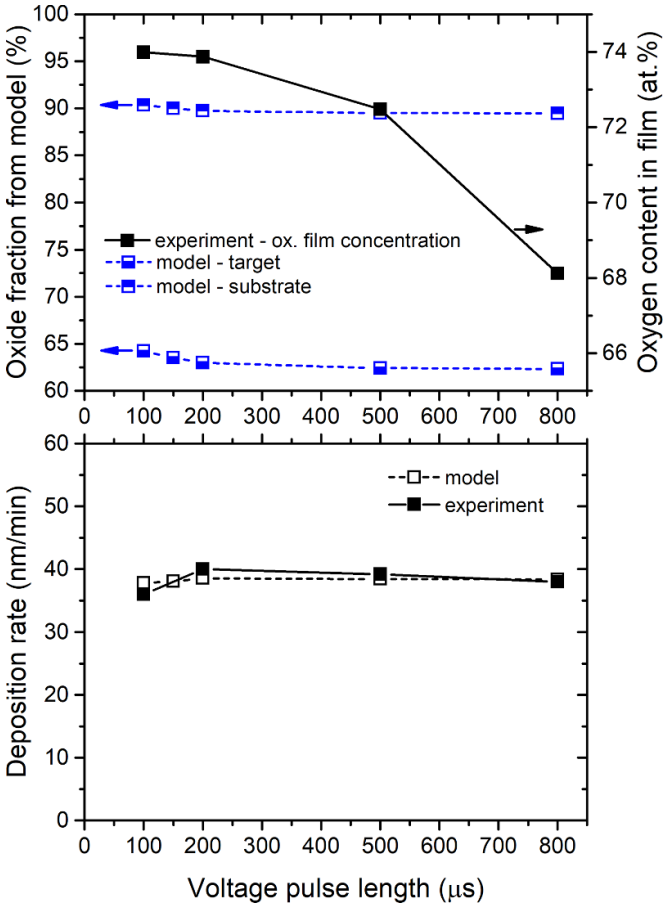

Figure 10. Top panel: calculated oxide fraction (dashed lines) on the substrate (half-up symbols) and the target (half-down symbols) and experimentally measured oxygen content in the film (solid lines) as a function of t_{on} at constant $p_{ox} = 0.25$ Pa. Bottom panel: calculated (dashed line) and experimentally measured (solid line) deposition rate as a function of t_{on} at constant $p_{ox} = 0.25$ Pa.

of metal atoms increases with increasing target power density, see figure 9. The model estimates the degree of W ionization in the discharge plasma during the pulse to increase from 50% to 80% when S_{da} increases from 100 to 500 W cm^{-2}.

Although this ion return effect is also present in r-HiPIMS, the situation is more complicated. First, the film density depends on the film composition and, thus, the deposition rate of metal atoms does not exactly correspond to the deposition rate of films measured in nm/min. Second, the sputtering rate of metal atoms from the target is affected by its oxide coverage which can, in principle, be either increasing or decreasing with the increase in S_{da}, depending on the complex balance between metal sputtering and oxygen implantation.

It is interesting that both the deposition rate and film oxygen concentration decrease with increasing S_{da} simultaneously. In other words, despite the fact that films (as well as the target, according to the model – see target oxide fraction in figure 7) are more metallic for higher S_{da}, the deposition rate is lower compared with lower S_{da}. This is in contrast to the situation in conventional DC, RF or mid-frequency reactive magnetron sputtering where the decrease in oxygen content in the film is always connected with an increase in deposition rate [47]. Again, this is a consequence of the increased return of W^+ ions onto the target, which effectively lowers the flux of W atoms onto the substrate.

As mentioned above, the deposition rate in the case of the high-oxygen regime slightly increases with increasing S_{da}, which is the opposite behaviour to that observed in the low-oxygen regime. The calculated deposition rate remains practically constant with increased S_{da}, in general. This is also related to the above-discussed fact that the flux of W onto the substrate is practically constant for the increasing S_{da}. However, there is a momentary increase in the calculated deposition rate for S_{da} increasing from 200 to 300 W cm^{-2}, which is also observed in the experimental results. For the target power density of 300 W cm^{-2}, the model shows a slight increase in the W flux onto the substrate, which leads to a decrease in the oxide fraction on the substrate and a small increase in the deposition rate.

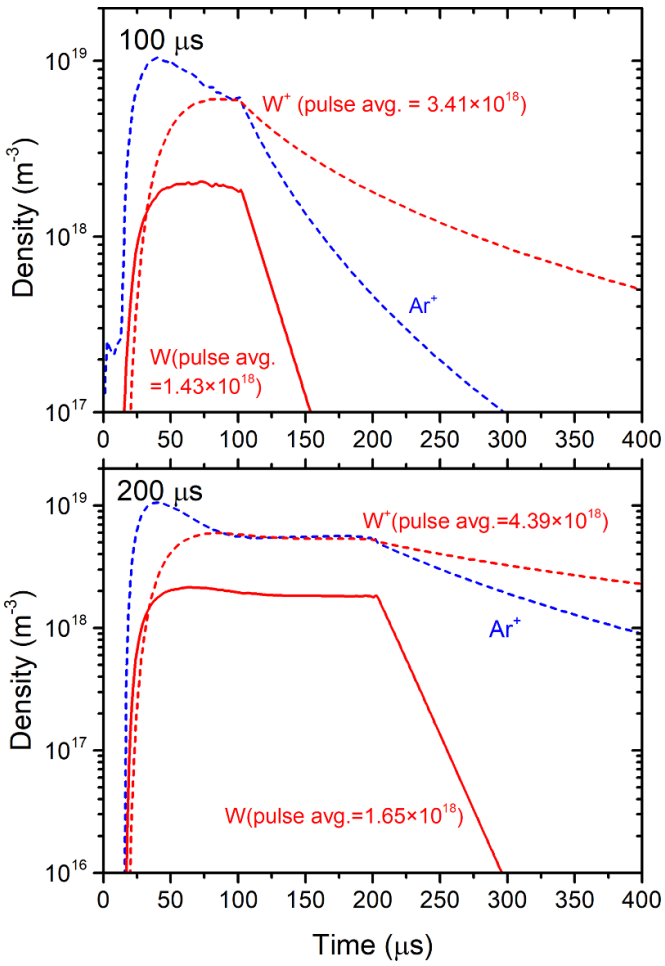

Figure 11. Calculated time evolutions of Ar^+, W and W^+ densities in the IR in front of the target for $t_{on} = 100$ μs (upper box) and $t_{on} = 200$ μs (bottom box) at $p_{ox} = 0.25$ Pa. Calculated pulse-averaged density for W and W^+ is given.

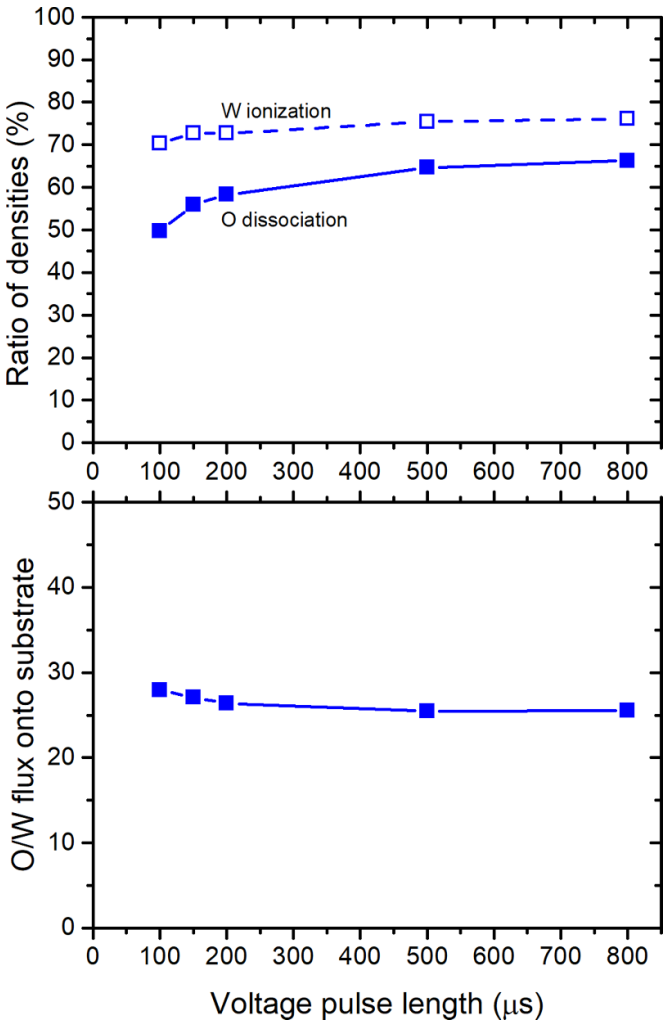

Figure 12. Top panel: calculated degree of W atom ionization (dashed line) and O_2 dissociation (solid line) as a function of t_{on} at $p_{ox} = 0.25$ Pa. Bottom panel: calculated ratio of oxygen and tungsten particle fluxes (atoms and ions) onto the substrate as a function of t_{on} at $p_{ox} = 0.25$ Pa.

3.3. Voltage pulse length effect

Finally, we report on the effect of voltage pulse length, t_{on}, (at constant $p_{ox} = 0.25$ Pa, constant $S_{da} \sim 250$ W cm^{-2} and constant period-averaged target power density of 2.35 W cm^{-2}). Thus, we have varied the repetition frequency to keep both pulse- and period-averaged target power densities constant. This complements the previous section where S_{da} was varied at constant t_{on}. The main results are presented in figure 10. The deposition rate slightly increases from 35 to 40 nm min^{-1} when t_{on} increases from 100 to 200 μs. The same trends were presented, for example, by [48, 49] in r-HiPIMS depositions of HfO_2 and WO_3 when t_{on} increases from 80 to 200 μs. This is also in very good agreement with the deposition rate calculated by the model. This could be caused by the lower total amount of W and W^+ particles produced during the pulse for $t_{on} = 100$ μs (see values of mean particle densities in figure 11). There is always a time delay between the start of the voltage pulse and the production of sputtered/ionized target particles. In our case, this delay is approximately 20 μs for all voltage pulse lengths, so there is practically no sputtering up to 20 μs into the pulse, i.e. up to 20% of the pulse-on time is 'wasted' for $t_{on} = 100$ μs, while it is only 10% for $t_{on} = 200$ μs and it further decreases for longer pulse lengths. The slight decrease in deposition rate from 40 to 38 nm min^{-1} when t_{on} is increased from 200 to 800 μs (also visible in the calculated trend, see figure 10 bottom panel) is caused mostly by a higher degree of ionization of sputtered W atoms (see figure 12 top panel) and thus more pronounced ion return of W^+ onto the target.

A monotonous decrease in C_{ox} from 74.0 at.% to 68.1 at.% is observed (figure 10) with increasing t_{on} from 100 to 800 μs. Presumably, this increases the film mass density, which might also explain the abovementioned decrease in the deposition rate for voltage pulse length increasing up to 800 μs.

For the increasing voltage pulse length, the simulations predict a slightly decreasing oxide fraction (figure 10 top panel) on the target and substrate, i.e. the films tend to be more metallic. This is in qualitative agreement with the experiment, although the decrease in oxide fraction in the substrate is not nearly as pronounced as the experimental oxygen content in

the film. We suggest that (reactive) gas rarefaction in front of the target due to the sputtering wind effect can cause this more pronounced decrease in film stoichiometry. This effect is not included in the simulation due to its spatial complexity.

The pulse-averaged degree of W ionization and O dissociation, as calculated by the model, are shown in figure 12 (top panel). The increase in W ionization facilitates increased metallization of the target as a result of more ions returning to the target. The bottom panel of the figure shows that the ratio of O/W atoms arriving onto the substrate decreases with increasing t_{on}, which results in the observed decrease of O content in the films.

4. Conclusion

The presented results show the successful application of a model combining an r-HiPIMS model with a discharge plasma model for the IR. It was used in conjunction with experimental results obtained for r-HiPIMS of WO_x films. The main results could be summarized as follows. It was found that there is a fundamental difference between reactive DC and HiPIMS of WO_x films. In the case of DC, the deposition rate decreases with oxygen partial pressure (as expected) whereas it is almost constant for HiPIMS deposition. A higher value of pulse-averaged target power density (at constant voltage pulse length) leads to a decrease in oxygen content in the film for both low- and high-oxygen regime. The deposition rate slightly decreases for the low-oxygen regime whereas it slightly increases for the high-oxygen regime (confirmed by the model quantitatively), mostly due to the lower amount of W^+ and thus lower losses caused by the ion return effect. Finally, it was found that longer voltage pulses lead to lower oxygen content in the film, probably due to more effective oxygen rarefaction caused by the sputtering wind. For short pulse (<100 μs), the deposition rate is lowered due to a significant role of 'wasted' time (~20 μs; time delay between creation of the plasma discharge and release of a significant amount of W atoms from the target). For longer pulses (>200 μs), there is a higher degree of W atom ionization and thus the deposition rate is lowered due to a more pronounced ion return effect.

Acknowledgments

This work was supported by the Czech Science Foundation under Project No. 19-14011S.

ORCID iDs

J Rezek https://orcid.org/0000-0002-2698-8753
S Haviar https://orcid.org/0000-0001-6926-8927

References

[1] Belosludtsev A, Houška J, Vlček J, Haviar S, Čerstvý R, Rezek J and Kettner M 2017 Structure and properties of Hf-O-N films prepared by high-rate reactive HiPIMS with smoothly controlled composition *Ceram. Int.* **43** 5661–7
[2] Vlček J, Belosludtsev A, Rezek J, Houška J, Čapek J, Čerstvý R and Haviar S 2016 High-rate reactive high-power impulse magnetron sputtering of hard and optically transparent HfO_2 films *Surf. Coat. Technol.* **290** 58–64
[3] Rezek J, Vlček J, Houška J and Čerstvý R 2014 High-rate reactive high-power impulse magnetron sputtering of Ta-O-N films with tunable composition and properties *Thin Solid Films* **566** 70–7
[4] Rezek J, Novák P, Houška J, Pajdarová A D and Kozák T 2019 High-rate reactive high-power impulse magnetron sputtering of transparent conductive Al-doped ZnO thin films prepared at ambient temperature *Thin Solid Films* **679** 35–41
[5] Hovsepian P E and Ehiasarian A P 2019 Six strategies to produce application tailored nanoscale multilayer structured PVD coatings by conventional and high power impulse magnetron sputtering (HIPIMS) *Thin Solid Films* **688** 137409
[6] Hovsepian P E, Ehiasarian A P, Purandare Y P, Mayr P, Abstoss K G, Mosquera Feijoo M, Schulz W, Kranzmann A, Lasanta M I and Trujillo J P 2018 Novel HIPIMS deposited nanostructured CrN/NbN coatings for environmental protection of steam turbine components *J. Alloys Compd.* **746** 583–93
[7] Vlček J, Rezek J, Houška J, Čerstvý R and Bugyi R 2013 Process stabilization and a significant enhancement of the deposition rate in reactive high-power impulse magnetron sputtering of ZrO_2 and Ta_2O_5 films *Surf. Coat. Technol.* **236** 550–6
[8] Rezek J, Houška J, Procházka M, Haviar S, Kozák T and Baroch P 2018 In-Ga-Zn-O thin films with tunable optical and electrical properties prepared by high-power impulse magnetron sputtering *Thin Solid Films* **658** 27–32
[9] Berg S, Blom H-O, Larsson T and Nender C 1987 Modeling of reactive sputtering of compound materials *J. Vac. Sci. Technol.* A **5** 202
[10] Berg S and Nyberg T 2005 Fundamental understanding and modeling of reactive sputtering processes *Thin Solid Films* **476** 215–30
[11] Kubart T, Kappertz O, Nyberg T and Berg S 2006 Dynamic behaviour of the reactive sputtering process *Thin Solid Films* **515** 421–4
[12] Güttler D, Abendroth B, Grötzschel R, Möller W and Depla D 2004 Mechanisms of target poisoning during magnetron sputtering as investigated by real-time *in situ* analysis and collisional computer simulation *Appl. Phys. Lett.* **85** 6134–6
[13] Depla D, Heirwegh S, Mahieu S and De Gryse R 2007 Towards a more complete model for reactive magnetron sputtering *J. Phys. D: Appl. Phys.* **40** 1957–65
[14] Strijckmans K, Schelfhout R and Depla D 2018 Tutorial: hysteresis during the reactive magnetron sputtering process *J. Appl. Phys.* **124** 241101
[15] Kozák T and Vlček J 2016 A parametric model for reactive high-power impulse magnetron sputtering of films *J. Phys. D: Appl. Phys.* **49** 055202
[16] Kozák T and Vlček J 2017 Dynamics of processes during the deposition of ZrO_2 films by controlled reactive high-power impulse magnetron sputtering: a modelling study *J. Appl. Phys.* **122** 043304
[17] Kadlec S and Čapek J 2017 Return of target material ions leads to a reduced hysteresis in reactive high power impulse magnetron sputtering: model *J. Appl. Phys.* **121** 171910
[18] Strijckmans K, Moens F and Depla D 2017 Perspective: is there a hysteresis during reactive high power impulse magnetron sputtering (R-HiPIMS)? *J. Appl. Phys.* **121** 080901
[19] Lundin D, Gudmundsson J T, Brenning N, Raadu M A and Minea T M 2017 A study of the oxygen dynamics in a

reactive Ar/O_2 high power impulse magnetron sputtering discharge using an ionization region model *J. Appl. Phys.* **121** 171917
[20] Kubart T and Andersson J 2012 Modelling of target effects in reactive HIPIMS *IOP Conf. Ser.: Mater. Sci. Eng.* **39** 012008
[21] Haviar S, Čapek J, Batková Š, Kumar N, Dvořák F, Duchoň T, Fialová M and Zeman P 2018 Hydrogen gas sensing properties of WO_3 sputter-deposited thin films enhanced by on-top deposited CuO nanoclusters *Int. J. Hydrog. Energy* **43** 22756–64
[22] Kumar N, Čapek J and Haviar S 2020 Nanostructured $CuWO_4/WO_{3-x}$ films prepared by reactive magnetron sputtering for hydrogen sensing *Int. J. Hydrog. Energy* **45** 18066–74
[23] Kumar K U, Bhat S D and Subrahmanyam A 2019 Electrochromic device with magnetron sputtered tungsten oxide (WO_3) and nafion membrane: performance with varying tungsten oxide thickness- a report *Mater. Res. Express.* **6** 045513
[24] Wang W Q, Wang X L, Xia X H, Yao Z J, Zhong Y and Tu J P 2018 Enhanced electrochromic and energy storage performance in mesoporous WO_3 film and its application in a bi-functional smart window *Nanoscale* **10** 8162–9
[25] Kalanur S S, Heo J, Yoo I H and Seo H 2017 2D WO_3 decorated with Pd for rapid gasochromic and electrical hydrogen sensing *Int. J. Hydrog. Energy* **42** 16901–8
[26] Kozák T and Pajdarová A D 2011 A non-stationary model for high power impulse magnetron sputtering discharges *J. Appl. Phys.* **110** 103303
[27] Čapek J and Kadlec S 2017 Return of target material ions leads to a reduced hysteresis in reactive high power impulse magnetron sputtering: experiment *J. Appl. Phys.* **121** 171911
[28] Kubart T and Aijaz A 2017 Evolution of sputtering target surface composition in reactive high power impulse magnetron sputtering *J. Appl. Phys.* **121** 171903
[29] Mutzke A, Schneider R, Eckstein W and Dohmen R 2011 SDTrimSP Version 5.00
[30] Houska J and Kozak T 2020 Distribution of O atoms on partially oxidized metal targets, and the consequences for reactive sputtering of individual metal oxides *Surf. Coat. Technol.* **392** 125685
[31] Kozák T, Vlček J and Kos Š 2013 Transport and ionization of sputtered atoms in high-power impulse magnetron sputtering discharges *J. Phys. D: Appl. Phys.* **46** 105203
[32] Huo C, Lundin D, Gudmundsson J T, Raadu M A, Bradley J W and Brenning N 2017 Particle-balance models for pulsed sputtering magnetrons *J. Phys. D: Appl. Phys.* **50** 354003
[33] Hajihoseini H, Cada M, Hubička Z, Ünaldi S, Raadu M A, Brenning N, Gudmundsson J T and Lundin D 2019 The effect of magnetic field strength and geometry on the deposition rate and ionized flux fraction in the HiPIMS discharge *Plasma* **2** 201–21
[34] Gudmundsson J T 2002 Notes on the electron excitation rate coefficients for argon and oxygen discharge (http://raunvisindastofnun.hi.is/sites/raunvisindastofnun.hi.is/files/rh-21-2002.pdf)
[35] Blanco F, da Silva F F, Limão-Vieira P and García G 2017 Electron scattering cross section data for tungsten and beryllium atoms from 0.1–5000 eV *Plasma Sources Sci. Technol.* **26** 085004
[36] Krishnakumar E and Srivastava S K 1992 Cross-sections for electron impact ionization of O_2 *Int. J. Mass Spectrom. Ion Process.* **113** 1–12
[37] Gudmundsson J T 2004 A critical review of the reactions set for a low pressure oxygen processing discharge (https://raunvisindastofnun.hi.is/sites/raunvisindastofnun.hi.is/files/rh-17-2004.pdf)
[38] Lee C 1994 Global model of plasma chemistry in a high density oxygen discharge *J. Electrochem. Soc.* **141** 1546
[39] Bowes M and Bradley J W 2014 The behaviour of negative oxygen ions in the afterglow of a reactive HiPIMS discharge *J. Phys. D: Appl. Phys.* **47** 265202
[40] Behrish R 1983 *Sputtering by Particle Bombardment II* (Berlin: Springer) (https://doi.org/10.1007/3-540-12593-0)
[41] Hemberg A, Dauchot J-P, Snyders R and Konstantinidis S 2012 Evaporation-assisted high-power impulse magnetron sputtering: the deposition of tungsten oxide as a case study *J. Vac. Sci. Technol.* A **30** 040604
[42] Hala M, Capek J, Zabeida O, Klemberg-Sapieha J E and Martinu L 2012 Hysteresis-free deposition of niobium oxide films by HiPIMS using different pulse management strategies *J. Phys. D: Appl. Phys.* **45** 055204
[43] Anders A, Andersson J and Ehiasarian A 2007 High power impulse magnetron sputtering: current-voltage-time characteristics indicate the onset of sustained self-sputtering *J. Appl. Phys.* **102** 113303
[44] Gudmundsson J T, Brenning N, Lundin D and Helmersson U 2012 High power impulse magnetron sputtering discharge *J. Vac. Sci. Technol.* A **30** 030801
[45] Kozák T and Lazar J 2018 Gas rarefaction in high power impulse magnetron sputtering: comparison of a particle simulation and volume-averaged models *Plasma Sources Sci. Technol.* **27** 115012
[46] Anders A 2010 Deposition rates of high power impulse magnetron sputtering: physics and economics *J. Vac. Sci. Technol.* A **28** 783–90
[47] Musil J, Baroch P, Vlček J, Nam K H and Han J G 2005 Reactive magnetron sputtering of thin films: present status and trends *Thin Solid Films* **475** 208–18
[48] Ganesan R, Murdoch B J, Treverrow B, Ross A E, Falconer I S, Kondyurin A, McCulloch D G, Partridge J G, McKenzie D R and Bilek M M M 2015 The role of pulse length in target poisoning during reactive HiPIMS: application to amorphous HfO_2 *Plasma Sources Sci. Technol.* **24** 035015
[49] Ganesan R, Akhavan B, Partridge J G, McCulloch D G, McKenzie D R and Bilek M M M 2017 Evolution of target condition in reactive HiPIMS as a function of duty cycle: an opportunity for refractive index grading *J. Appl. Phys.* **121** 171909